First-Principles Investigation of 2D o-Al_2C_2 Monolayer
A High-Performance Anode for Li/Na–Ion Batteries

Agouri, Mohamed; Benaddi, Ayoub; Khossossi, Nabil; El Filali, Said; Abbassi, Abderrahman; Hasnaoui, Abdellatif; Taj, Souad; Manaut, Bouzid

DOI
10.1002/cphc.202500025

Publication date
2025

Document Version
Final published version

Published in
ChemPhysChem

ChemPhysChem

Research Article
doi.org/10.1002/cphc.202500025

Chemistry Europe
European Chemical Societies Publishing

www.chemphyschem.org

First-Principles Investigation of 2D o-Al_2C_2 Monolayer: A High-Performance Anode for Li/Na–Ion Batteries

Mohamed Agouri, Ayoub Benaddi, Nabil Khossossi, Said El Filali, Abderrahman Abbassi,* Abdellatif Hasnaoui, Souad Taj, and Bouzid Manaut

The development of novel anode materials with superior electrochemical performance is imperative for advancing next-generation high-performance rechargeable batteries beyond current limitations. In this study, it presents a 2D o-Al_2C_2 monolayer as a promising lightweight candidate for lithium and sodium–ion battery systems, based on the density functional theory investigations and ab initio molecular dynamics (AIMD) simulations. Our comprehensive investigation demonstrates that the o-Al_2C_2 monolayer exhibits remarkable stability with a cohesive energy of -5.30 eV atom^{-1} and maintains its structural integrity at room temperature during extended AIMD simulations. The o-Al_2C_2 monolayer demonstrates exceptional electrochemical characteristics for Li and Na storage: theoretical specific capacities of 3780.42 and 3436.75 mA h g^{-1}, optimal average open circuit voltages of 0.81 and 0.67 V, and favorable diffusion barriers of 0.62 eV and 0.31 eV, respectively. These performance metrics significantly surpass those of conventional graphite (372 mA h g^{-1}) and other recently reported 2D anode materials, establishing o-Al_2C_2 as an exceptionally promising candidate for next-generation energy storage applications. Hence, this current theoretical investigation suggests that the o-Al_2C_2 monolayer holds significant potential for future experimental studies in lithium and sodium storage applications for LIB and NIB systems.

1. Introduction

Secondary batteries dominate current energy storage technologies available on the market. Rechargeable lithium–ion batteries (LIBs), in particular, are extensively used in electric vehicles and portable electronic devices owing to their high energy density.[1,2] Despite their widespread adoption, current lithium–ion battery systems face critical limitations that hinder their applicability for emerging large-scale energy storage needs. The increasing demand for electrical energy applications, including electric vehicles and large-scale storage systems, is placing stringent performance requirements on LIBs. This heightened demand for lithium resources is driving up costs and exposing several challenges associated with current LIB systems, including high prices, safety concerns, and limited resource availability, making them less suitable for large scale use.[3–5] Although lithium and sodium have similar chemical and physical properties in energy storage, sodium offers a more attractive alternative due to its abundance and lower cost. Despite sodium's higher atomic weight and a standard electrode potential of about 0.3 V, which affects the energy density of sodium–ion batteries (NIBs) compared to LIBs, NIBs present significant potential for energy storage applications, particularly for power grids. Hence, while NIBs currently compete with LIBs in consumer electronics, the NIBs hold considerable promise for broader energy storage applications.[6–10] The transition from lithium to sodium-based systems represents a paradigm shift in battery technology development, requiring innovative electrode materials that can efficiently accommodate larger sodium–ions while maintaining structural integrity and electrochemical performance.

In the pursuit of advanced electrode materials, 2D structures have emerged as promising candidates owing to their unique advantages: shortened ion diffusion pathways, increased active surface sites, enhanced structural flexibility, and tunable electronic properties. Recently, significant attention and effort have been devoted to the development of alternative anode materials for LIB and NIB systems, leading to notable advancements. Among these alternatives, 2D materials have emerged as some of the most promising candidates owing to their large surface area and exceptional physical and chemical properties compared to their bulk forms.[11,12] These characteristics allow 2D materials to exhibit excellent electrochemical performance, including high energy densities. Various 2D materials, including graphene, borophene, black/blue phosphorus, MXenes, and transition metal

M. Agouri, S. El Filali, A. Abbassi, S. Taj, B. Manaut
Laboratory of Research in Physics and Engineering Sciences
Polydisciplinary Faculty
Sultan Moulay Slimane University
Beni Mellal 23000, Morocco
E-mail: Abderrahman.abbassi@usms.ac.ma

A. Benaddi, A. Hasnaoui
Polydisciplinary Faculty of Khouribga
LS2ME Laboratory
Sultan Moulay Slimane University
B.P. 145, Khouribga 25000, Morocco

N. Khossossi
Department of Materials Science and Engineering
Faculty of Mechanical, Maritime and Materials Engineering
Delft University of Technology
Mekelweg 2, 2628 CD Delft, The Netherlands

A. Abbassi
Associate Member of the Laboratory for Materials, Energy, and Environment
Faculty of Sciences Semlalia
Cadi Ayyad University
Marrakech 40000, Morocco

oxides, sulfides, and their composite structures, have been extensively studied through both theoretical and experimental approaches as potential anode materials for LIBs and NIBs.[13–18] However, many of these 2D materials still face challenges, such as limited specific capacity, poor charge–discharge efficiency, instability, and high manufacturing costs.[19] Hence, the ongoing development of advanced 2D materials with enhanced electrochemical performance continues to be a critical focus and priority for enhancing LIB and NIB technologies. Graphite, the most commonly used anode material in LIBs, while stable and cost-effective, suffers from limited capacity that constrains further development. Alternative candidates like germanene, silicon, and carbon nanotubes offer higher specific capacities but continue to face challenges related to instability and internal deformation that affect safety and battery life.[20–24]

At present, extensive theoretical and experimental investigations have been conducted on hexagonal 2D materials, particularly the III–V binary monolayer group.[25] These materials are considered one of the most innovative classes in anode design in LIB/NIB systems owing to their interesting physicochemical properties. Among them, the hexagonal boron nitride monolayer (h-BN) has gained significant attention for its potential applications in nanoelectronics. However, due to its large band gap energy and weak interaction with Li/Na–ions, the h-BN monolayer is unsuitable as an active anode material in LIB/NIB systems.[26–28] In contrast, other hexagonal structures including h-AlN, h-BP, h-BSb, and h-BAs have emerged as promising candidates for anode materials with large theoretical specific capacities.[29–32] Additionally, the h-AlC monolayer has been theoretically investigated, revealing favorable properties for Li and Na adsorption. Notably, Chodvadiya et al.[33] demonstrated that 2D h-AlC exhibits a high specific capacity of ≈739.61 mAh g^{-1} for Li and 397.58 mAh g^{-1} for Na, along with a low diffusion barrier, making it a prospective material for anode applications in NIB and LIB systems. Recently, a new polymorph of 2D III–V orthorhombic monolayers has been proposed by Zhao et al.[34] through first-principles calculations, establishing the theoretical foundation for materials with distinct structural symmetries and electronic properties compared to their hexagonal counterparts. Initial investigations into orthorhombic variants such as o-B_2N_2, o-B_2P_2, and o-Al_2N_2 have shown promising results for energy storage applications.[35–38]

Inspired by these advancements, we present, for the first time, a comprehensive investigation of the o-Al_2C_2 monolayer as a promising anode material for LIB and NIB systems. Using DFT and AIMD computations, we systematically analyze the structural stability, electronic properties, adsorption energetics, ion diffusion, and theoretical capacity of this novel material. Our findings reveal that the o-Al_2C_2 monolayer demonstrates exceptional theoretical specific capacities of 3780.42 mAh g^{-1} for lithium and 3436.75 mAh g^{-1} for sodium—significantly higher than current state-of-the-art anode materials. The material exhibits favorable adsorption energies, optimal voltage profiles, and suitable diffusion barriers, while maintaining metallic conductivity during ion insertion. These characteristics, combined with the material's lightweight composition and structural stability, position o-Al_2C_2 as a transformative candidate for next-generation energy storage technologies. Compared to other 2D materials previously reported as negative electrode materials, the new orthorhombic-Al_2C_2 shows great potential as a promising anode material with a high theoretical specific capacity, making it well-suited for future experimental investigations in advanced battery systems.

2. Computational Details

All first-principles calculations in this work were performed within the framework of DFT as implemented in the Quantum ESPRESSO code.[39,40] We employed the Perdew–Burke–Ernzerhof functional within the generalized gradient approximation to describe the exchange-correlation interactions.[41] The projected augmented wave method was utilized to treat the electron–ion interactions.[42] To ensure the accuracy and convergence of our calculations, we conducted extensive convergence tests for both energy cutoff and k-point sampling. The plane wave expansion had a cutoff energy of 884.37 eV (65 Ry) and the Brillouin zone was sampled using Monkhorst–Pack k-point meshes of $8 \times 16 \times 1$ and $16 \times 32 \times 1$ for the structural optimization and the electronic properties calculations, respectively. These parameters provided total energy convergence to within 10^{-5} eV. All atomic structures were fully relaxed until the Hellmann–Feynman forces on each atom were less than 10^{-4} eV $Å^{-1}$. The energy and force convergence criteria for self-consistency were set to 10^{-6} and 10^{-4} eV $Å^{-1}$, respectively. To account for van der Waals interactions, we applied the Grimme D2 approach.[43] A 20 Å vacuum along the *z*-axis was introduced to avoid interactions between the studied system and its periodic images.

For systems involving lithium and sodium adsorption, we employed a $2 \times 3 \times 1$ supercell containing 12 aluminum and 12 carbon atoms to minimize the interaction between periodic images of adsorbed ions. The charge density difference (CDD) plots were generated with a dense grid of $140 \times 140 \times 200$ points to ensure high-resolution visualization. Charge transfer from lithium/sodium atoms on the monolayer was computed using the Bader charge analysis.[44] Structural visualization was performed using Vesta and XCrySDen software.[45,46] The electronic density of states (DOS) was calculated using the tetrahedron method with Blöchl corrections and a dense k-point mesh of $24 \times 48 \times 1$ to ensure accurate representation of the electronic structure. The dynamical stability of the o-Al_2C_2 monolayer was verified by calculating phonon dispersion along the high symmetry directions $\Gamma - X - S - Y - \Gamma$ with phonopy code.[47] The force constants for phonon calculations were obtained using the density functional perturbation theory method on a $4 \times 4 \times 1$ q-point mesh. This approach allows for accurate prediction of lattice dynamics and thermal properties from first principles.

The thermodynamic stability of the system was assessed by calculating the cohesive energy using the equation.[48]

$$E_{\text{coh}} = \frac{E_{o-Al_2C_2} - 2(E_{Al} + E_C)}{4} \quad (1)$$

where $E_{o-Al_2C_2}$ represents the total energy of the unit cell of o-Al_2C_2. $E_{Al,C}$ is the total energies of individual atoms in a cubic

system ($a = 20$ Å). The thermal stability of the o-Al_2C_2 monolayer was investigated using AIMD simulations in the canonical ensemble (NVT) with a Nosé–Hoover thermostat. We employed a time step of 1 fs for a total simulation time of 12 ps at 300 K, which is sufficient to evaluate the structural integrity at room temperature. The temperature oscillations and structural evolution were monitored throughout the simulation to assess thermal stability. To determine the minimum energy path and the activation energy barrier for the diffusion of each adsorbent on the o-Al_2C_2 monolayer, we used the climbing-image nudged elastic-band (CI-NEB) method.[49] For each diffusion pathway, we employed seven intermediate images between the initial and final states, with spring constants of 5.0 eV Å^{-2} between adjacent images. All images were relaxed until forces perpendicular to the path were less than 0.02 eV Å^{-1}, ensuring accurate determination of transition states and energy barriers. For open-circuit voltage (OCV) calculations, we considered various lithium and sodium concentrations to determine the most stable configurations and corresponding formation energies. The theoretical specific capacity was calculated based on the maximum number of adsorbed ions while maintaining favorable binding energies. The volume changes during ion insertion were estimated by comparing the optimized structures before and after ion adsorption, providing insights into the material's structural stability during charge–discharge cycles.

3. Results and Discussion

3.1. Theoretical Stability and Electronic Properties

3.1.1. Theoretical Stability

The o-Al_2C_2 monolayer features a distinct orthorhombic structure with unique bonding characteristics that differentiate it from previously investigated 2D materials. We conducted a comprehensive structural analysis using an orthorhombic unit cell containing two aluminum and two carbon atoms, arranged in a planar configuration similar to graphene, h-AlC, and o-Al_2N_2 monolayers.[18,33,37] The structure features a hexagonal arrangement with alternating Al—C bonds forming a stable network that optimizes electron sharing between the elements, contributing to its notable stability despite the difference in electronegativities between Al and C atoms. Our optimized structural parameters reveal lattice constants of $a = 6.28$ Å and $b = 3.14$ Å, with interatomic distances of 2.54, 1.98, and 1.33 Å for Al—Al, Al—C, and C—C bonds, respectively. These values align with prior reports, though bond lengths differ slightly from o-Al_2N_2 due to atomic radii differences between N and C. The shorter C—C bond (1.33 Å vs 1.48 Å for N-N in o-Al_2N_2) reflects stronger covalent character, contributing to the overall rigidity and stability of the o-Al_2C_2 framework. Our findings are in complete agreement with previously reported studies.[33,37] The slight differences in bond lengths observed, compared to other materials such as o-Al_2N_2, are attributed to the difference in atomic radii between nitrogen and carbon.

To establish the viability of o-Al_2C_2 as a candidate for experimental synthesis and practical applications, we conducted rigorous theoretical stability assessments through three complementary approaches: thermodynamic stability via cohesive energy calculations, dynamical stability through phonon dispersion analysis, and thermal stability using ab initio molecular dynamics simulations. This multifaceted stability evaluation is essential for predicting the material's behavior under realistic conditions in energy storage applications. The interdependence of these stability criteria provides a comprehensive understanding of the material's potential performance across different operational environments, from room temperature to elevated temperatures that might be encountered in battery applications. Additionally, the stability analysis offers insights into potential synthesis pathways, suggesting that chemical vapor deposition or molecular beam epitaxy might be viable approaches for experimental realization of this promising 2D material. Verifying the theoretical stability for the potential experimental synthesis of the studied 2D material o-Al_2C_2 is necessary. For this reason, we first examined its thermodynamic stability by calculating its cohesive energy using Equation (1). As shown in **Table 1**, the obtained cohesive energy indicates favorable thermodynamic stability and suggests a strong bonding network. These findings are in good agreement and comparable to other reported works, particularly for o-Al_2N_2, o-B_2X_2 (X = N,P), and h-AlC monolayers.[33,37,38] Additionally, the E_{coh} of the studied material was found to be −5.30 eV atom^{-1}, which falls within the range of other 2D materials that have been experimentally and theoretically investigated, including graphene (−7.6 eV), silicene (−4.57 eV), phosphorene (−3.18 eV), Mg_2C (−3.43 eV atom^{-1}), and Mn_2C (−3.35 eV atom^{-1}).[50–54]

The dynamical stability of o-Al_2C_2 was rigorously evaluated by calculating its phonon dispersion spectrum along high-symmetry paths in the first Brillouin zone (Γ-X-S-Y-Γ). As illustrated in **Figure 1**b, the phonon dispersion curves exhibit no imaginary frequencies throughout the Brillouin zone, conclusively confirming the dynamical stability of the monolayer structure. This absence of soft phonon modes indicates that the o-Al_2C_2 monolayer represents a local minimum in the potential energy surface and would maintain its structural integrity under small perturbations. The phonon spectrum reveals three acoustic branches (one longitudinal and two transverse modes) and nine optical branches, consistent with the 12 vibrational degrees of freedom expected from the four atoms in the primitive cell. The phonon DOS shown in Figure 1d provides further insights into the vibrational properties, with distinct peaks

Table 1. Structural parameters and thermodynamic stability of o-Al_2C_2 monolayer compared with similar 2D materials. The lattice constants (*a, b*), interatomic distances (III–III, III–V, V–V), and cohesive energies (E_{coh}) demonstrate the favorable stability of o-Al_2C_2 relative to other reported structures. The more negative cohesive energy of o-Al_2C_2 compared to h-AlC indicates enhanced thermodynamic stability, while the slightly less negative value compared to o-Al_2N_2 reflects the different bonding nature between C and N atoms.

Material	a [Å]	b [Å]	$d_{III-III}$	d_{III-V}	d_{V-V}	E_{coh} [eV atom^{-1}]
o-Al_2C_2	6.28	3.14	2.54	1.98	1.33	−5.30
o-Al_2N_2[37]	5.90	3.11	2.55	1.82	1.48	−5.59
h-AlC[33]	3.36	3.36	–	1.93	–	−4.95

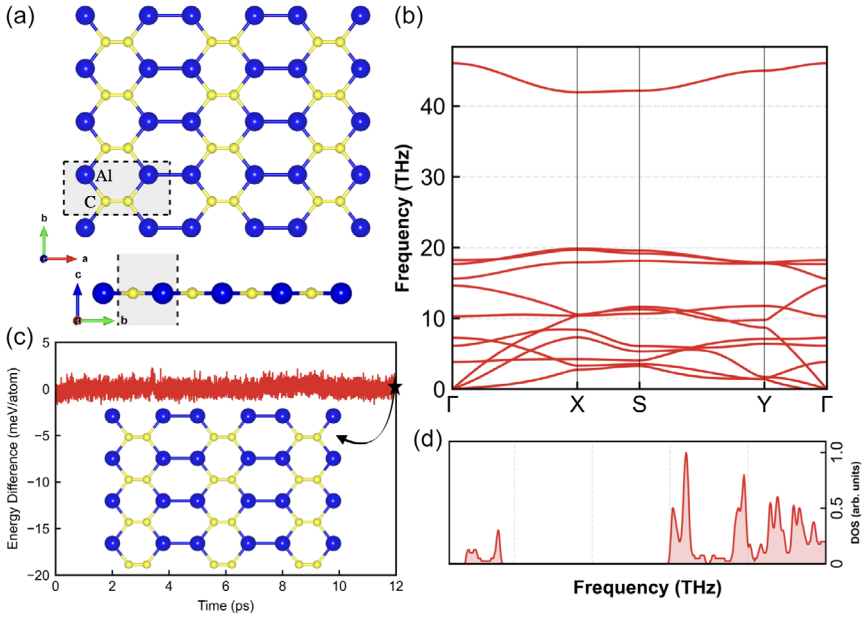

Figure 1. a) Top and side views of the *o*-Al_2C_2 monolayer with the unit cell indicated by a dashed rectangle. Blue and yellow spheres represent the Al and C atoms, respectively. b) Phonon dispersion curve along high-symmetry paths (Γ-X-S-Y-Γ) in the first Brillouin zone, showing no imaginary frequencies and confirming dynamical stability. c) Energy fluctuation during ab initio molecular dynamics simulation at 300 K over 12 ps with an inset showing the preserved structure after simulation, demonstrating excellent thermal stability at room temperature. d) Calculated phonon DOS showing the vibrational distribution of the *o*-Al_2C_2 monolayer with characteristic peaks at ≈3, 12, and 18 THz.

indicating well-defined vibrational modes. Notably, the higher frequency modes (above 15 THz) primarily involve carbon atoms due to their lighter mass compared to aluminum, while the lower frequency region is dominated by collective vibrations involving both Al and C atoms. This separation in vibrational signatures contributes to the material's thermal properties and potential phonon-mediated electron transport characteristics.

To further verify the thermal stability of o-Al_2C_2 under realistic temperature conditions, we performed extended AIMD simulations at 300 K for a duration of 12 ps. Figure 1c displays the evolution of the total energy throughout the simulation period, showing only minor fluctuations around the equilibrium value, which is characteristic of a thermally stable system. Detailed structural analysis of the AIMD trajectory reveals that the o-Al_2C_2 monolayer maintains its structural integrity without significant distortions, bond breaking, or reconstruction events. The inset structure shown at the 12 ps timepoint demonstrates that the hexagonal arrangement of atoms remains intact, with Al—C bonds preserving their original configuration throughout the simulation, further confirming the robust structural stability of the monolayer. This thermal stability at room temperature is especially significant for practical applications in battery systems, where thermal management is a critical consideration for long-term performance and safety. The combined evidence from cohesive energy calculations, phonon dispersion analysis, and AIMD simulations provides strong, multifaceted support for the theoretical stability of the o-Al_2C_2 monolayer, suggesting its viability for experimental synthesis and potential integration into energy storage devices.

Furthermore, to elucidate the mechanical properties of the anisotropic material, we calculated the elastic constants, Young's modulus, and Poisson's ratio along the *x*- and *y*-directions using the energy-strain method, considering strain values ranging from −0.03 to 0.03 with increments of 0.005. The calculated results are presented in **Table 2**, which also compares our material with other monolayers of the same crystal structure. As shown in the table, the calculated elastic constants satisfy the criteria for mechanical stability, which are as follows: $C_{11} > 0$, $C_{22} > 0$, $C_{66} > 0$, and $C_{11}C_{22} - C_{12}^2 > 0$. These conditions are essential for ensuring that the material remains mechanically stable under deformation. To further understand the material's behavior, we computed Poisson's ratios and Young's moduli. The calculated Poisson's ratios indicate anisotropic behavior in the material. The value $V_x = 0.19$ suggests a greater lateral contraction in the *y*-direction compared to $V_y = 0.081$ in the *x*-direction, meaning that the material exhibits a stronger coupling between deformations along these axes. Similarly, the Young's moduli confirm directional stiffness differences. The material is significantly stiffer in the *x*-direction ($Y_x = 169$) than in the *y*-direction ($Y_y = 73$), highlighting its anisotropic mechanical response.

Table 2. A comparative analysis of the elastic constants (C_{11}, C_{12}, C_{22}, and C_{66}), along with young's modulus and Poisson's ratio in the *x*- and *y*-directions, for 2D o-Al_2C_2 material, in comparison with o-Al_2N_2 and *o*-B_2N_2 orthorhombic monolayers.

Property/system	*o*-Al_2C_2	*o*-Al_2N_2[37]	*o*-B_2N_2[35]
C_{11} [N m^{-1}]	171	145	250
C_{12} [N m^{-1}]	14	28	35
C_{22} [N m^{-1}]	74	143	291
C_{66} [N m^{-1}]	42	44	21
$Y_x - Y_y$ [N m^{-1}]	169–73	143–141	246–286
$V_x - V_y$	0.19–0.08	0.19–0.19	0.12–0.14

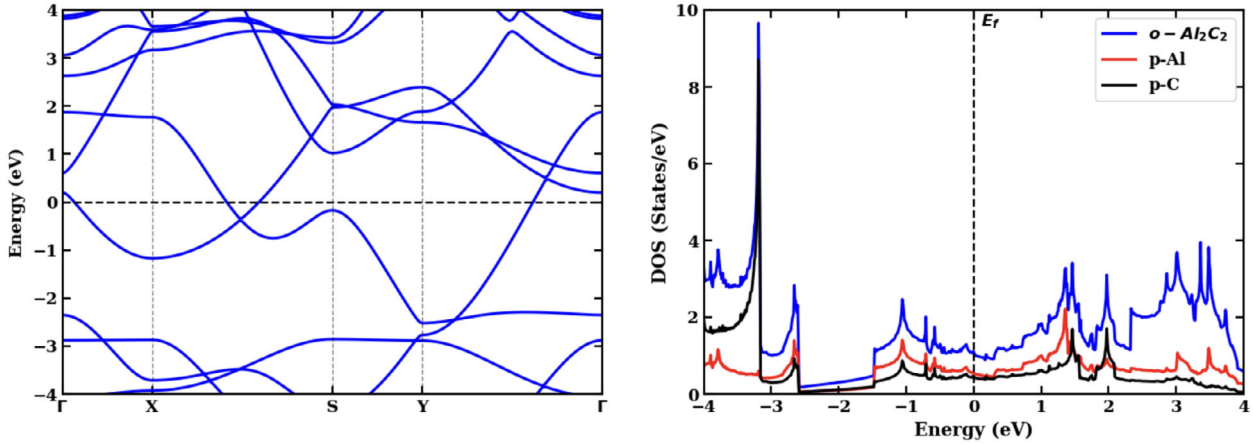

Figure 2. Electronic properties of pristine *o*-Al_2C_2 monolayer: electronic band structure (left) showing band crossing at the Fermi level, indicating metallic behavior; and partial/total DOS (right) revealing significant contributions from Al and C *p*-orbitals at the Fermi energy, responsible for the material's intrinsic conductivity.

3.1.2. Electronic Properties

The electronic properties of electrode materials directly influence their performance in battery systems, particularly affecting charge transport kinetics during ion insertion/extraction processes. We performed detailed electronic structure calculations to elucidate the fundamental electronic characteristics of the o-Al_2C_2 monolayer. **Figure 2** presents the electronic band structure along high-symmetry paths in the Brillouin zone and the corresponding DOS. The band structure reveals a significant overlap between the valence and conduction bands at the Fermi level, unambiguously demonstrating the intrinsic metallic character of o-Al_2C_2. This metallic nature is particularly advantageous for electrode applications as it facilitates efficient electron transport without activation barriers, potentially enabling rapid charge/discharge processes in battery systems. Analysis of the partial DOS (PDOS) provides deeper insights into the electronic structure, revealing that the metallicity primarily originates from the *p*-orbitals of both aluminum and carbon atoms, which contribute significantly to the states at the Fermi level. The strong hybridization between Al and C states indicates robust covalent bonding in the structure, consistent with the high cohesive energy calculated previously. This intrinsic metallic conductivity of o-Al_2C_2 represents a significant advantage over many other 2D materials being considered for battery applications, particularly semiconducting materials that may require additional conductive additives to achieve satisfactory performance in practical devices.

3.2. Adsorption Energy of Lithium/Sodium on o-Al_2C_2 Monolayer

The interaction between electrode materials and alkali metal ions is a critical determinant of battery performance metrics, including specific capacity, cycling stability, and rate capability. To systematically evaluate the potential of o-Al_2C_2 as an anode material, we conducted a comprehensive investigation of lithium and sodium adsorption energetics on the monolayer surface. We examined multiple potential adsorption sites considering the symmetry and electronic structure of the orthorhombic lattice. As illustrated in **Figure 3**, we identified and characterized three distinct categories of adsorption sites: 1) hollow sites (H_1 and H_2) located above the centers of Al_2C_4 and Al_4C_2 hexagons respectively; 2) bridge sites (B_1, B_2, and B_3) positioned along Al—Al, Al—C, and C—C bonds; and 3) top sites (T_{Al} and T_C) directly above

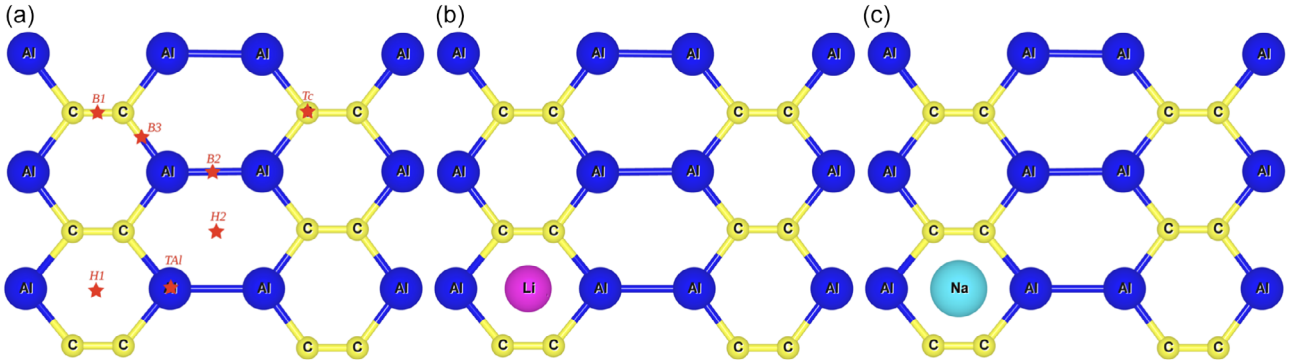

Figure 3. Lithium and sodium adsorption configurations on *o*-Al_2C_2 monolayer: a) schematic representation of the possible adsorption sites on the *o*-Al_2C_2 surface, including hollow sites (H_1, H_2), bridge sites (B_1, B_2, B_3), and top sites (T_{Al}, T_C), and b,c) optimized geometries of Li and Na atoms at the most energetically favorable H_1 site, showing the equilibrium binding heights.

individual Al and C atoms. For each site, we performed full geometric optimization to determine the most energetically favorable configurations for Li and Na adsorption.

The adsorption energetics were quantitatively evaluated using density functional theory calculations with the equation.

$$E_{Ads} = E_{M+Al_2C_2} - E_{Al_2C_2} - E_M \quad (2)$$

where $E_{M+Al_2C_2}$ and $E_{Al_2C_2}$ represent the total energies of the systems with and without the adsorbed M = Li, Na atoms, respectively. $E_{M=Li,Na}$ refers to the energy of a single Li/Na atom in its bulk structure. This formulation provides a robust measure of the interaction strength between the adsorbed ions and the substrate, with more negative values indicating stronger binding. Strong but not excessive binding is desirable for battery applications—providing sufficient structural stability during cycling while allowing for reversible ion insertion/extraction processes.

Our computational results, summarized in **Table 3**, reveal that among all considered sites, the H_1 hollow site (located above the Al_2C_2 hexagon) exhibits the most favorable adsorption energies for both Li and Na atoms, with values of −1.28 and −1.11 eV, respectively. The H_2 site presents the second most favorable configuration, with notably weaker binding energies of −0.41 eV for Li and −0.82 eV for Na. The optimized geometries in Figure 3b,c illustrate the equilibrium binding configurations, with Li positioned at a height of 1.59 Å and Na at 2.07 Å above the monolayer at the H_1 site, reflecting the different ionic radii of these alkali metals. During optimization, we observed that ions initially placed at bridge or top sites generally migrated toward the more stable hollow positions, confirming the energetic preference for adsorption at hollow sites. Significantly, the adsorption energies obtained for o-Al_2C_2 substantially exceed those reported for other promising 2D anode materials, including o-Al_2N_2 (−0.39/−0.23 eV), o-B_2P_2 (−0.705/−0.603 eV), and o-B_2N_2 (−1.408/−0.569 eV).[35–37] These comparatively strong adsorption energies suggest that o-Al_2C_2 may offer superior ion storage capability and cycling stability in practical battery applications.

The highly favorable adsorption at the H_1 site can be rationalized through an examination of the electronic interactions between the adsorbed ions and the substrate. The preferential binding at hollow sites is attributed to the optimal coordination environment provided by the surrounding atoms, which maximizes the orbital overlap between the *s*-orbitals of alkali metals and the delocalized π-electrons of the monolayer. Bader charge analysis reveals significant charge transfer from Li/Na atoms to the o-Al_2C_2 substrate, with transferred charges of ≈0.874 $|e|$ for Li and 0.872 $|e|$ for Na, indicating the predominantly ionic nature of the bonding. This extensive charge transfer is facilitated by the large electronegativity difference between the alkali metals and the substrate atoms, with the transferred electrons occupying the available states near the Fermi level of the metallic o-Al_2C_2 monolayer.

Table 3. Energetics and structural parameters for li and Na adsorption on *o*-Al_2C_2 monolayer. The table presents adsorption energies (E_{Ads}) and equilibrium binding heights (h) for the two most favorable adsorption sites, demonstrating the strong interaction between alkali metal ions and the *o*-Al_2C_2 surface.

System	Adsorption site	Adsorption energy E_{Ads} [eV]	Binding height h [Å]
Li@$Al_{12}C_{12}$	H_1	−1.28	1.59
	H_2	−0.41	1.70
Na@$Al_{12}C_{12}$	H_1	−1.11	2.07
	H_2	−0.82	2.22

3.3. Electronic Conductivity and Charge Density

The electronic conductivity of electrode materials during ion insertion and extraction processes is a critical determinant of battery performance, particularly affecting rate capability and power density. To comprehensively evaluate the electronic properties of o-Al_2C_2 under realistic operating conditions, we investigated the changes in electronic structure following lithium and sodium adsorption at the most favorable H_1 site. **Figure 4** presents the calculated electronic band structures and DOS for both Li- and Na-adsorbed systems. Remarkably, our analysis reveals that the metallic character of pristine o-Al_2C_2 is fully preserved after alkali metal adsorption, as evidenced by the persistent band crossing at the Fermi level and non-zero DOS. This maintenance of metallic conductivity throughout the ion insertion process represents a significant advantage for battery applications, potentially enabling high-rate performance by facilitating rapid electron transport during charging and discharging operations.

Detailed analysis of the PDOS provides deeper insights into the electronic properties of the alkali metal-adsorbed systems. For both Li- and Na-adsorbed o-Al_2C_2, the states near the Fermi level arise primarily from the *p*-orbitals of carbon and aluminum atoms, with additional contributions from the s-orbitals of the adsorbed alkali metals. This orbital hybridization between the substrate and the adsorbed ions facilitates efficient charge transfer and strong binding interactions. The maintenance of metallic conductivity after ion adsorption stands in favorable contrast to some other anode materials that undergo metal-to-semiconductor transitions upon ion insertion, which can detrimentally affect their electrochemical performance. The preserved metallicity in o-Al_2C_2 aligns with observations in other high-performance 2D anode materials, including h-AlN, g-GeC, AlP_3, o-Al_2N_2, o-B_2N_2, and o-B_2P_2,[29,35–37,55,56] suggesting a general trend among promising orthorhombic 2D materials for battery applications.

To elucidate the fundamental mechanisms governing the interaction between alkali metal ions and the o-Al_2C_2 substrate, we conducted a detailed analysis of the spatial charge redistribution upon adsorption. **Figure 5** presents the 3D CDD plots for both Li and Na adsorption, calculated using the equation.

$$\Delta\varrho = \varrho_{M@Al_2C_2} - \varrho_{Al_2C_2} - \varrho_{M=Li,Na} \quad (3)$$

where $\varrho_{M@Al_2C_2}$ and $\varrho_{Al_2C_2}$ represent the electronic charge densities of the system with and without one M = Li/Na atom adsorbed on the o-Al_2C_2, respectively. The $\varrho_{M=Li,Na}$ is the electronic charge density of a single M = Li/Na atom in an isolated system with the same cell volume. The CDD visualizations provide striking evidence of substantial charge transfer from the alkali metals

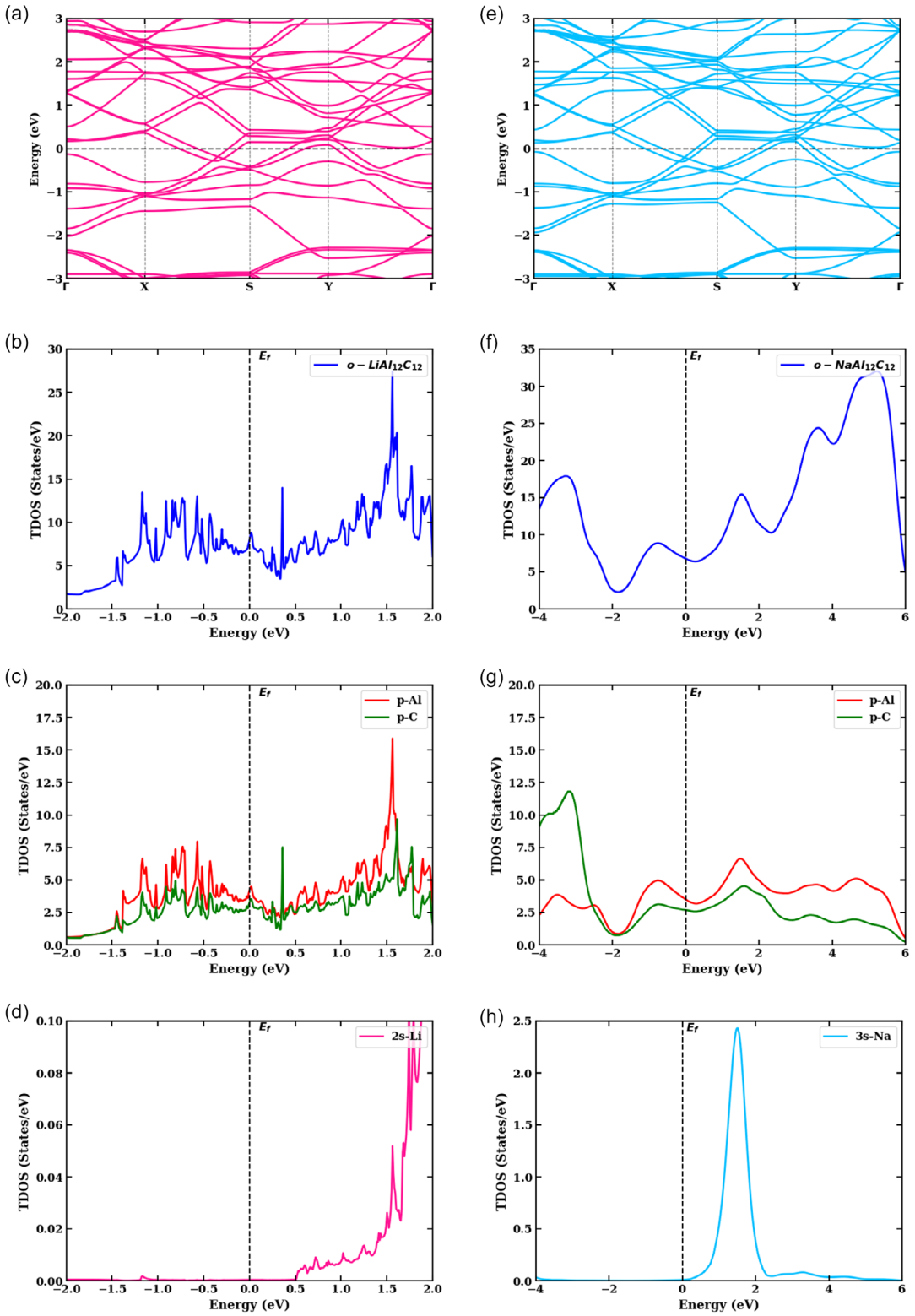

Figure 4. Electronic properties of *o*-Al_2C_2 monolayer after alkali metal adsorption: a–d) electronic band structure, total DOS, and partial DOS for Li adsorbed at the H_1 site and e–h) corresponding electronic structure data for Na adsorption. Both systems maintain metallic character, demonstrating robust electronic conductivity during ion insertion.

to the o-Al_2C_2 substrate, with regions of charge accumulation (brown) and depletion (cyan) clearly demarcated. For both Li and Na adsorption, we observe significant charge depletion around the alkali metal atoms and pronounced charge accumulation distributed across the surrounding carbon and aluminum atoms of the monolayer. Quantitative Bader charge analysis confirms this qualitative observation, revealing substantial charge transfers of 0.874 $|e|$ for Li and 0.872 $|e|$ for Na. These

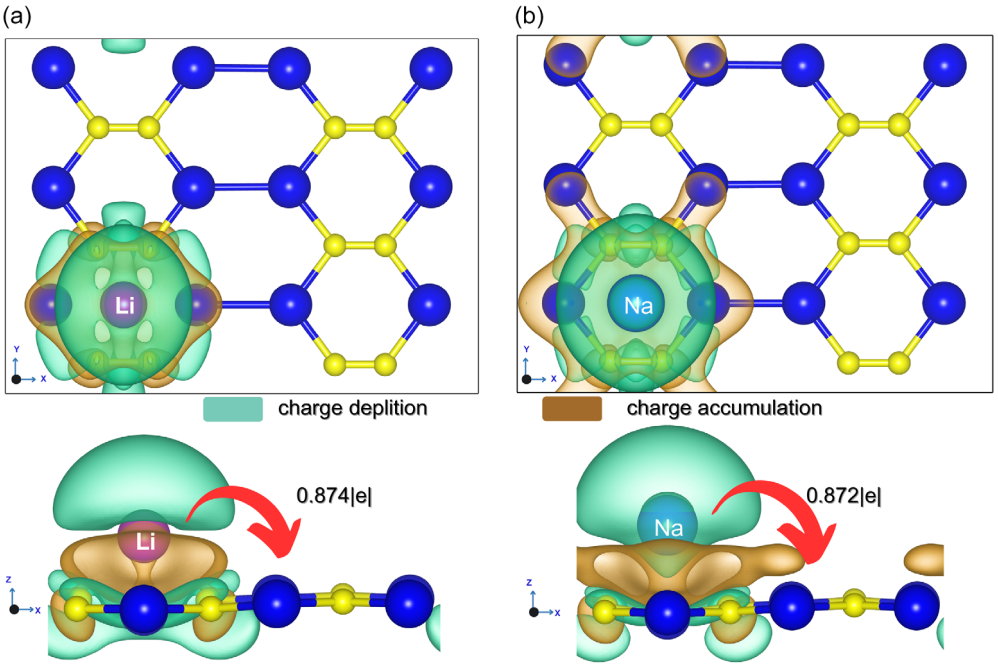

Figure 5. CDD analysis for alkali metal adsorption on *o*-Al_2C_2 monolayer: top and side views of the CDD for a) Li and b) Na ions adsorbed at the H_1 site. Brown regions represent electron accumulation, while cyan regions indicate electron depletion. Bader charge analysis reveals substantial charge transfers of 0.874 and 0.872 $|e|$ for Li and Na, respectively, demonstrating the predominantly ionic nature of the binding interaction.

values approach the theoretical maximum of one electron per alkali metal atom, indicating nearly complete ionization of the adsorbed species. The extensive charge transfer can be attributed to the considerable electronegativity difference between the alkali metals and the substrate elements, with the transferred electrons primarily populating the delocalized π-system of the o-Al_2C_2 monolayer. The similar charge transfer magnitudes for Li and Na suggest comparable binding mechanisms despite their different atomic sizes, which may contribute to the material's versatility for both LIB and NIB applications. This substantial charge transfer not only strengthens the binding interaction but also maintains the metallic conductivity of the system, as the transferred electrons contribute to the delocalized states near the Fermi level.

3.4. Diffusion of Li/Na–Ions on o-Al_2C_2

Ion diffusion kinetics within electrode materials fundamentally determines the rate capability and high-power performance of rechargeable batteries. To comprehensively evaluate the potential of o-Al_2C_2 for practical battery applications, we conducted detailed investigations of lithium and sodium diffusion pathways and associated energy barriers using the CI-NEB method. This rigorous computational approach allows for precise determination of minimum energy pathways and transition states during ion migration across the monolayer surface. Based on the symmetry of the o-Al_2C_2 structure, we identified and analyzed three distinct diffusion pathways, as illustrated in **Figure 6**a: path 1 along the zigzag direction (*a*-axis), path 2 along the armchair direction (*b*-axis), and path 3 traversing over the less favorable H_2 hollow site. For each pathway, we calculated the complete energy profile to quantify the diffusion barriers that ions must overcome during migration between adjacent favorable adsorption sites.

The calculated energy profiles for the three diffusion pathways, presented in Figure 6b,c, reveal significant insights into the ion transport properties of o-Al_2C_2. For both lithium and sodium, path 1 (along the zigzag direction) exhibits the lowest energy barrier, with calculated values of 0.62 eV for Li and 0.31 eV for Na. These values are notably favorable compared to path 2 (0.79 eV for Li and 0.47 eV for Na) and path 3 (0.93 eV for Li and 0.58 eV for Na). The preferential diffusion along path 1 can be attributed to the shorter migration distance and more favorable transition state configuration, where the migrating ion maintains stronger coordination with the substrate atoms throughout the diffusion process. The significantly lower diffusion barrier for sodium compared to lithium (approximately half the value) is particularly noteworthy and can be explained by the different electronic structures and ionic radii of these species. The larger ionic radius of Na+ results in a greater distance from the substrate surface, reducing the strength of interaction with the surface atoms and consequently lowering the energy barrier for migration. This disparity in diffusion barriers suggests that o-Al_2C_2 may exhibit superior rate performance in NIBs compared to lithium–ion systems, a finding that could have significant implications for high-power NIB applications.

Comparing our calculated diffusion barriers with those of other reported 2D anode materials provides valuable context for assessing the potential performance of o-Al_2C_2 in practical battery applications. The lithium diffusion barrier of 0.62 eV in o-Al_2C_2 is notably lower than those reported for many other promising anode materials, including graphene (0.71 eV), h-AlC (0.76 eV), AlP_3 (0.74–0.85 eV), and h-BAs monolayer (0.68–0.83 eV).[32,33,56–61]

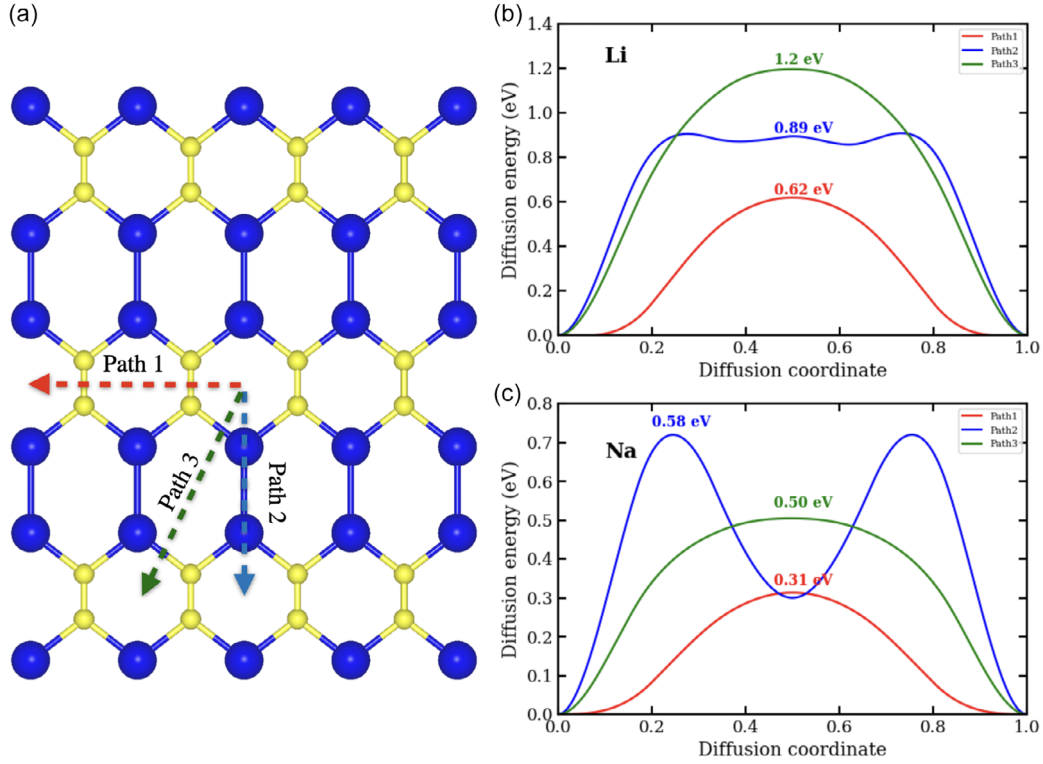

Figure 6. Diffusion pathways and energy barriers for Li and Na ions on the *o*-Al_2C_2 monolayer: a) schematic representation of the three identified diffusion pathways: path 1 along the zigzag direction, path 2 along the armchair direction, and path 3 across the H_2 site; b) energy profiles for Li ion diffusion along the three pathways; and c) corresponding energy profiles for Na ion diffusion, showing consistently lower barriers compared to Li.

Similarly, the sodium diffusion barrier of 0.31 eV compares favorably with values reported for other materials being considered for NIB applications. These comparatively low diffusion barriers are highly encouraging for battery applications, as they suggest that o-Al_2C_2 could support rapid charge/discharge processes, enhancing power density and rate capability in practical devices. The remarkably low sodium diffusion barrier of 0.31 eV is particularly significant given the growing interest in NIBs as more sustainable alternatives to lithium-based systems. This favorable Na diffusion kinetics positions o-Al_2C_2 as an especially promising candidate for next-generation high-performance NIB anodes.

3.5. Record-High Li/Na-Storage Capacity and Equilibrium Voltage

To comprehensively evaluate the potential of o-Al_2C_2 as an anode material for practical battery applications, we conducted detailed investigations of its theoretical storage capacity, OCV characteristics, and structural stability during ion insertion. We employed a methodical approach involving stepwise insertion of lithium and sodium atoms onto both sides of the monolayer, systematically filling the energetically favorable H_1 and H_2 sites. This sequential loading process began with uniform insertion at the most favorable H_1 site, forming the first adsorption layer ($M_{12}Al_{12}C_{12}$), followed by gradual occupation of the secondary H_2 sites, creating a series of intermediate configurations ($M_nAl_{12}C_{12}$) with increasing ion concentrations. For each configuration, we calculated the average binding energy to assess the thermodynamic stability and determine the maximum theoretical capacity that could be achieved while maintaining favorable energetics.

The average binding energy for each ion concentration was calculated using the formula.

$$E_b^{avg} = \frac{E_{M_n@Al_{12}C_{12}} - E_{o-Al_{12}C_{12}} - nE_M}{n} \quad (4)$$

where $E_{M_n@Al_{12}C_{12}}$ and $E_{o-Al_{12}C_{12}}$ represent the ground state energies of $M_n@Al_{12}C_{12}$ and o-$Al_{12}C_{12}$, respectively. $E_{M=Li/Na}$ refers to the energy of a single lithium/sodium–ion in the bulk phase. The calculated average binding energies for various lithium and sodium concentrations, presented in **Table 4**, reveal that the o-Al_2C_2 monolayer can accommodate a remarkably high number of alkali metal ions while maintaining favorable energetics. Specifically, our calculations show that the system can store up to 66 lithium atoms and 60 sodium atoms per 12 formula units of o-Al_2C_2 before the average binding energy becomes prohibitively weak. This extraordinary storage capacity can be attributed to the unique electronic structure of o-Al_2C_2, which facilitates efficient charge transfer and strong binding interactions with the adsorbed ions. The gradual decrease in binding strength with increasing ion concentration reflects the growing electrostatic repulsion between adjacent adsorbed ions, yet remarkably, the binding energy remains favorable (negative) even at very high loadings. This behavior suggests excellent cycling stability, as the strong binding prevents dendrite formation while remaining reversible for practical battery operation.

Table 4. Adsorption energetics of li and Na ions on the *o*-Al_2C_2 monolayer with increasing ion concentration. The consistently negative average binding energies, even at high loadings, demonstrate exceptional storage capacity and favorable energetics for battery applications.

Lithium		Sodium	
System	E_b^{avg} [eV]	System	E_b^{avg} [eV]
Li_1-$Al_{12}C_{12}$	−1.28	Na_1-$Al_{12}C_{12}$	−1.11
Li_2-$Al_{12}C_{12}$	−1.26	Na_2-$Al_{12}C_{12}$	−1.06
Li_4-$Al_{12}C_{12}$	−1.12	Na_4-$Al_{12}C_{12}$	−0.84
Li_6-$Al_{12}C_{12}$	−0.97	Na_6-$Al_{12}C_{12}$	−0.70
Li_{12}-$Al_{12}C_{12}$	−0.80	Na_{12}-$Al_{12}C_{12}$	−0.65
Li_{18}-$Al_{12}C_{12}$	−0.73	Na_{18}-$Al_{12}C_{12}$	−0.73
Li_{24}-$Al_{12}C_{12}$	−0.73	Na_{24}-$Al_{12}C_{12}$	−0.78
Li_{30}-$Al_{12}C_{12}$	−0.54	Na_{30}-$Al_{12}C_{12}$	−0.68
Li_{36}-$Al_{12}C_{12}$	−0.43	Na_{36}-$Al_{12}C_{12}$	−0.61
Li_{42}-$Al_{12}C_{12}$	−0.39	Na_{42}-$Al_{12}C_{12}$	−0.60
Li_{48}-$Al_{12}C_{12}$	−0.36	Na_{48}-$Al_{12}C_{12}$	−0.59
Li_{54}-$Al_{12}C_{12}$	−0.31	Na_{54}-$Al_{12}C_{12}$	−0.56
Li_{60}-$Al_{12}C_{12}$	−0.28	Na_{60}-$Al_{12}C_{12}$	−0.56
Li_{66}-$Al_{12}C_{12}$	−0.27	–	–

To further evaluate the thermal stability of o-Al_2C_2 under realistic battery operating conditions, we performed additional AIMD simulations at elevated temperatures of 400 K (127 °C) and 500 K (227 °C), which significantly exceed the typical working temperature range of LIBs and NIBs (up to 60–80 °C). As shown in **Figure 7**, both Li-intercalated and Na-intercalated o-Al_2C_2 systems maintain their structural integrity throughout the 10 ps simulation period at these elevated temperatures. The temperature profiles (Figure 7a,b) exhibit normal fluctuations around the target values (±50 K), as expected in NVT ensemble simulations with Nosé–Hoover thermostat. Notably, the energy evolution (Figure 7c,d) demonstrates small fluctuations (within ±20 meV atom^{-1}) without systematic drift after the initial equilibration period (first 2 ps), confirming the system has reached thermodynamic equilibrium. To quantitatively assess structural stability, we analyzed several key metrics: 1) root-mean-square displacement (RMSD) of the framework atoms relative to the initial configuration, 2) evolution of Al—C bond lengths, and 3) retention of the orthorhombic lattice parameters. The RMSD values remained below 0.2 Å for the Al_2C_2 framework at 400 K and below 0.3 Å at 500 K, indicating minimal structural distortion even at the highest temperature. The average Al—C

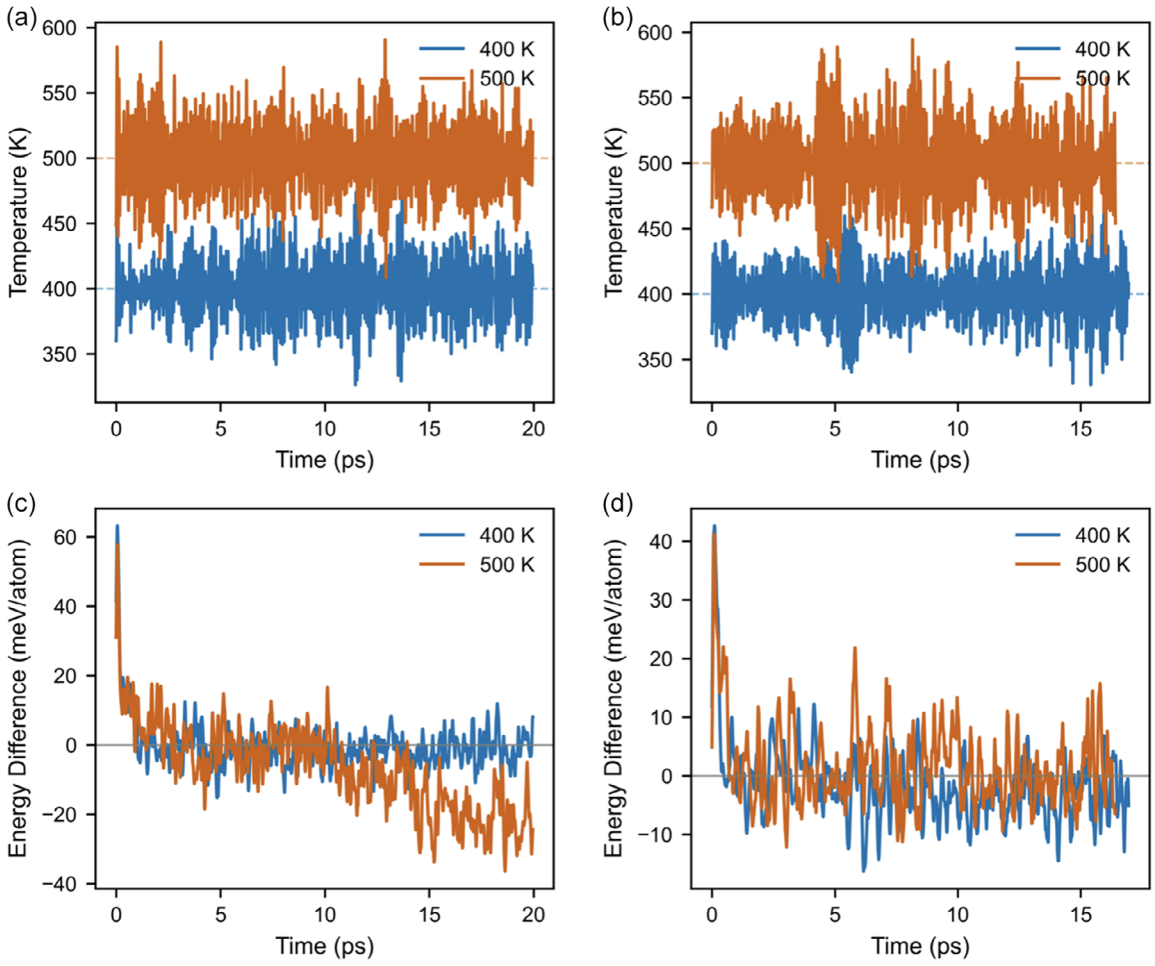

Figure 7. Thermal stability of *o*-Al_2C_2 monolayer at elevated temperatures: a,b) temperature evolution during 10 ps AIMD simulations at 400 and 500 K for Li-*o*-Al_2C_2 and Na-*o*-Al_2C_2 systems and c,d) corresponding energy fluctuations demonstrating thermodynamic equilibrium and structural integrity at these elevated temperatures.

bond length fluctuated within 5% of its equilibrium value (1.98 Å), demonstrating the robustness of the covalent bonding network. The preservation of the orthorhombic structure was confirmed by analyzing the angular distribution between lattice vectors, which maintained orthogonality throughout the simulation. The persistence of structural integrity at 500 K is particularly significant as it demonstrates thermal stability at temperatures nearly three times higher than typical battery operating conditions (60–80 °C), providing an exceptional safety margin for practical applications. Furthermore, the observed thermal stability correlates with the high cohesive energy (−5.30 eV atom^{-1}) and strong covalent bonding within the Al_2C_2 framework. This moderate thermal resilience can be attributed to the unique orthorhombic structure with its network of strong Al—C bonds, which create a rigid framework that resists thermal deformation. Unlike some 2D materials that undergo phase transitions or decomposition at elevated temperatures, o-Al_2C_2 exhibits remarkable thermal stability, making it particularly suitable for battery applications in demanding thermal environments, such as electric vehicles, where thermal management is a critical safety concern.

The OCV profiles, which directly influence battery performance metrics such as energy density and operating voltage, were calculated using the Nernst equation in a simplified form that neglects volume change, entropy, and pressure effects.

$$\mathrm{OCV} = \frac{-E_{M_{n_2}@Al_{12}C_{12}} + E_{M_{n_1}@Al_{12}C_{12}} + (n_2 - n_1)E_M}{e(n_2 - n_1)} \quad (5)$$

where $E_{M_{n_2}@Al_{12}C_{12}}$ and $E_{M_{n_1}@Al_{12}C_{12}}$ are the energies at n_2 and n_1 number of Li/Na-adsorbed on the 2D o-$Al_{12}C_{12}$ monolayer, respectively, and e is the electronic charge. To identify the thermodynamically stable states during ion insertion, we calculated formation energies for various ion concentrations using the following.

$$E_f = E_{M_n@Al_{12}C_{12}} - \left\{\frac{nE_{M_{n_{max}}@Al_{12}C_{12}} + (n_{max} - n)E_{o-Al_{12}C_{12}}}{n_{max}}\right\} \quad (6)$$

where $E_{M_n@Al_{12}C_{12}}$ and $E_{M_{n_{max}}@Al_{12}C_{12}}$ are the total energy for n Li/Na atoms and total energy of maximum Li/Na loaded o-$Al_{12}C_{12}$ monolayer, respectively. **Figure 8**a,b presents the formation energy as a function of ion concentration, revealing convex hull profiles that identify the thermodynamically stable intermediate phases during ion insertion. For lithium insertion, we identified five stable intermediate structures along the minimum energy path, while sodium insertion exhibited three stable intermediate configurations. These stable states represent the equilibrium compositions that would be observed during gradual charging/discharging processes in a practical battery system. The corresponding OCV profiles and average binding energies as functions of ion concentration are presented

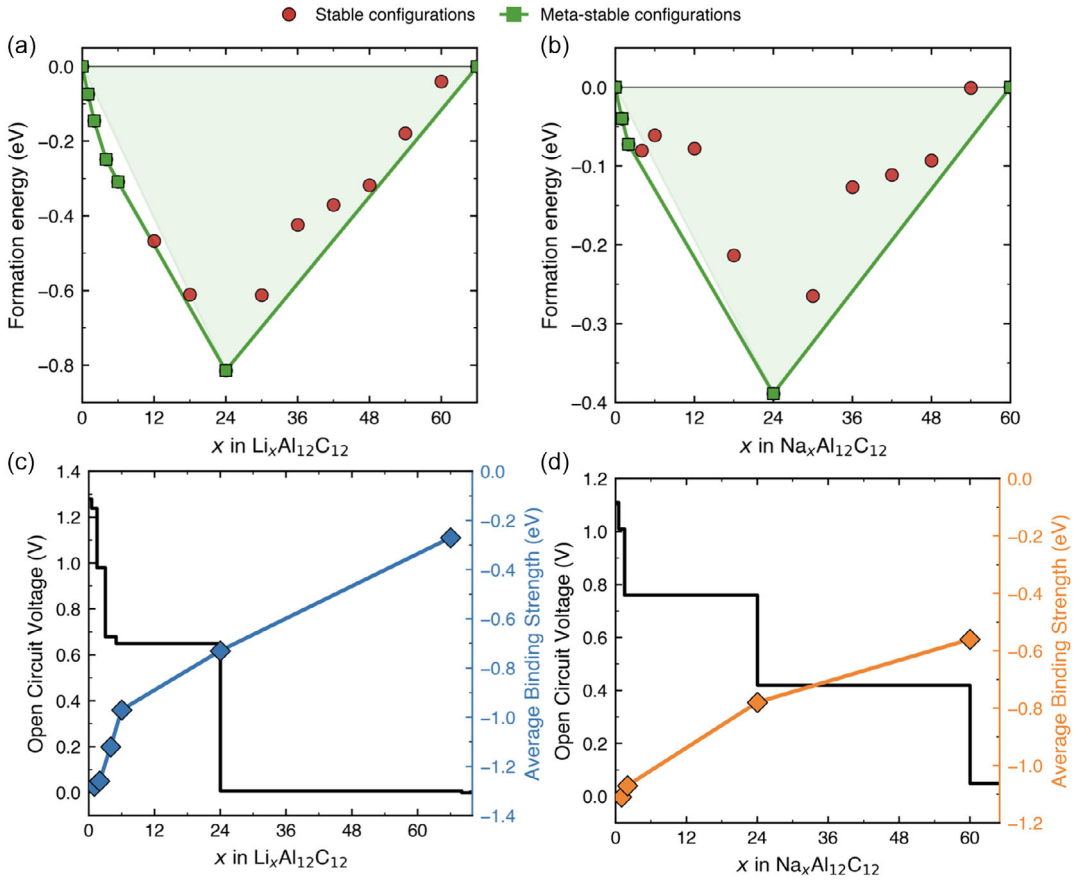

Figure 8. Electrochemical properties of o-Al_2C_2 for Li and Na storage: a,b) formation energy per formula unit as a function of ion concentration for Li and Na systems, identifying thermodynamically stable intermediate phases, and c,d) OCV profiles (black) and average binding energies (blue) as functions of Li and Na concentrations, demonstrating favorable voltage characteristics and binding energetics throughout the insertion process.

in Figure 8c,d, providing a comprehensive view of the electrochemical characteristics of the o-Al_2C_2 monolayer.

The calculated OCV profiles reveal highly favorable characteristics for battery applications. For both lithium and sodium systems, the average OCVs remain positive and below 1.5 V throughout the insertion process, with average values of ≈0.81 V for Li and 0.67 V for Na. This voltage range is ideal for anode materials, ensuring a suitable cell voltage when paired with conventional cathodes while avoiding undesirable side reactions such as electrolyte decomposition and solid-electrolyte interphase formation that typically occur at very low voltages. The slightly higher average voltage for lithium compared to sodium can be attributed to the stronger binding interactions in the Li system, consistent with the binding energy trends. The OCV profiles exhibit multiple distinct voltage plateaus corresponding to the stable intermediate phases identified in the formation energy analysis, suggesting a staged insertion mechanism that would contribute to good cycling stability. These voltage characteristics, combined with the strong binding energies, indicate excellent electrochemical performance potential for o-Al_2C_2 in both LIB and NIB applications.

Based on the maximum ion storage capacities identified in our calculations (66 Li atoms and 60 Na atoms per 12 formula units of o-Al_2C_2), we determined the theoretical specific capacity using the standard electrochemical formula.

$$C = \frac{n_{max}.F}{M_{o-Al_{12}C_{12}}} \quad (7)$$

where $M_{o-Al_{12}C_{12}}$ refers to the relative molecular mass of o-$Al_{12}C_{12}$ monolayer. n_{max} and F present the maximum number of Li/Na-adsorbed and Faraday constant. The calculated theoretical specific capacities are exceptionally high: 3780.42 mAh g^{-1} for lithium and 3436.75 mAh g^{-1} for sodium. These values far surpass those of conventional anode materials, including commercial graphite (372 mAh g^{-1}), and significantly exceed the capacities reported for other emerging 2D materials such as h-AlN, h-AlC, o-Al_2N_2, o-B_2P_2, and o-B_2N_2.[29,33,35–37] The extraordinary storage capacity of o-Al_2C_2 can be attributed to several factors: 1) its lightweight composition, leading to a low molecular weight denominator in the capacity calculation; 2) the presence of multiple energetically favorable adsorption sites on both sides of the monolayer; 3) the strong binding interactions that stabilize high ion concentrations; and 4) the robust electronic conductivity that facilitates charge transfer throughout the insertion process.

In addition to capacity and voltage characteristics, the structural stability during ion insertion is a critical consideration for practical battery applications, as excessive volume changes can lead to mechanical degradation and capacity fading. We evaluated the volume changes in the o-Al_2C_2 monolayer during lithium and sodium insertion by comparing the optimized structures at various ion concentrations. Remarkably, our calculations reveal minimal volume changes, with small shrinkages ranging between −0.41% and −6.48% for lithium and between −0.43% and −0.46% for sodium at maximum storage. These minimal volume changes are highly favorable for cycling stability and represent a significant advantage over many conventional anode materials that suffer from large volume expansions during ion insertion. For comparison, commercial graphite anodes typically experience volume changes of ≈10%, while silicon-based anodes can undergo expansions exceeding 300%. The exceptional structural stability of o-Al_2C_2 during ion insertion, combined with its extraordinary capacity and favorable voltage characteristics, positions this material as an exceptionally promising candidate for next-generation high-performance battery anodes.

Moreover, the storage capacity of o-Al_2C_2 monolayer surpasses that of previously reported anode materials for LIBs and NIBs, with a theoretical capacity ≈10 times greater than that of commercial graphite.[62] Additionally, the o-Al_2C_2 monolayer exhibits a significantly lower diffusion barrier compared to certain reported anode materials, including graphene, h-AlC, AlP_3, and h-BAs monolayer, ensuring excellent mobility of Li/Na-ions on the surface.[32,33,56,61] This facilitates the smooth operation of LIB and NIB systems, particularly for sodium–ion storage. To further validate our theoretical findings, we compare the electrochemical performance of o-Al_2C_2

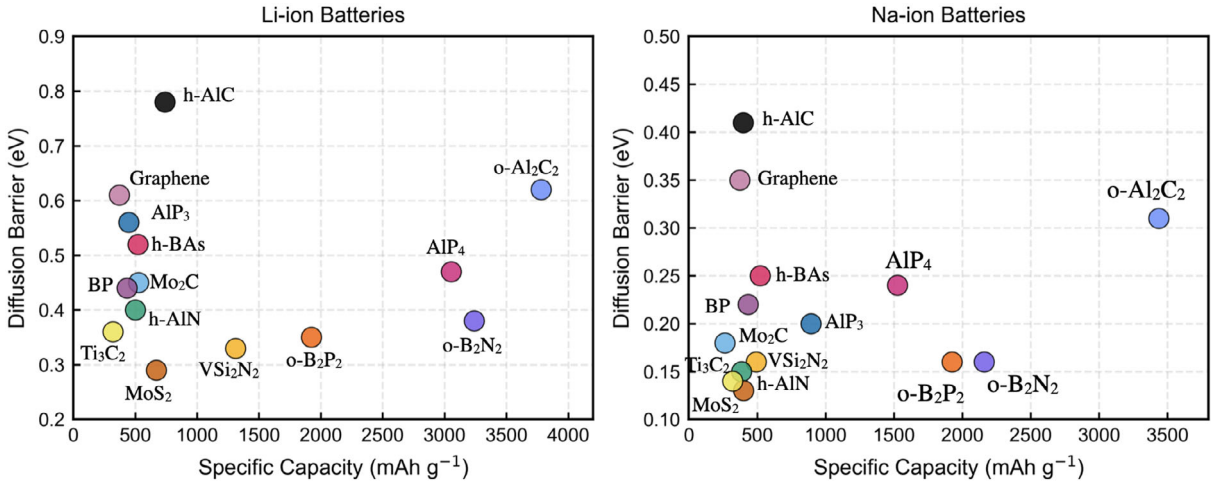

Figure 9. Comparative analysis of specific capacity and diffusion barrier for Li–ion and Na–ion storage in 2D materials: The chart highlights the exceptional storage capacity of *o*-Al_2C_2 for both Li and Na ions relative to other reported 2D materials, demonstrating its superior potential for next-generation battery applications.

with experimentally synthesized and theoretically predicted anode materials. Notably, MoS_2 has been experimentally demonstrated as a high-capacity anode material for LIBs, with a reported experimental capacity of ≈670 mAh g^{-1}.[63,64] Similarly, biphenylene has been investigated as a potential anode material for NIBs, with a predicted storage capacity of 1075.37 mAh g^{-1}.[65] In contrast, our theoretical calculations predict that o-Al_2C_2 can achieve an exceptionally high capacity of over 3000 mAh g^{-1}, significantly surpassing both MoS_2 and biphenylene. However, it should be pointed out that the predicted capacities from DFT calculations are typically larger than the experimental values. The overestimated theoretical capacities can be attributed to factors not considered in DFT calculations, such as defects, stacking layers, and side reactions between the electrode and electrolyte. These effects tend to reduce the overall performance in experimental setups, leading to a lower measured capacity.[66,67] Despite these considerations, the remarkably high theoretical capacity of o-Al_2C_2 highlights its strong potential as an anode material for next-generation LIBs and NIBs. A comparison of the o-Al_2C_2 monolayer's theoretical storage capacity with typical 2D anode materials for LIBs and NIBs, as highlighted in **Figure 9**, indicates that both systems offer high capacities and are well-suited for battery applications.[68,69] Overall, our findings demonstrate that orthorhombic Al_2C_2 material could be considered a promising anode material, characterized by a significant diffusion barrier and high storage capacity for LIBs and NIBs, with competitive advantages over experimentally verified anode materials.

4. Conclusion

In this work, we have conducted the first principle investigation of the orthorhombic-Al_2C_2 monolayer as a potential anode material for next-generation LIBs and NIBs, employing density functional theory calculations and ab initio molecular dynamics simulations. Our analysis confirms that o-Al_2C_2 is both thermodynamically and dynamically stable, with a cohesive energy of −5.30 eV $atom^{-1}$, absence of imaginary phonon frequencies, and excellent thermal stability throughout 12 ps of AIMD simulations at 300 K. Calculated adsorption energies reveal that the H_1 site at the Al_2C_4 hollow position is the most favorable, showcasing significant adsorption energies of −1.28 and −1.11 eV, respectively, for Li and Na. These adsorption energies substantially exceed those of previously reported 2D materials, including o-Al_2N_2 (−0.39/−0.23 eV) and o-B_2P_2 (−0.705/−0.603 eV), indicating stronger ion-substrate interactions and potential for enhanced cycling stability. Along the storage process, the o-Al_2C_2 monolayer demonstrates a significant average voltage and diffusion barrier, along with high specific capacities of ≈0.81 V, 0.62 eV, and 3780.42 mAh g^{-1} for Li and 0.67 V, 0.31 eV, and 3436.75 mAh g^{-1} for Na, which are substantially greater than those of commercial graphite and other recently studied 2D materials. Particularly notable is the theoretical capacity of o-Al_2C_2, which exceeds graphite by ≈10-fold and surpasses other promising 2D materials like h-AlC (739.61/397.58 mAh g^{-1}) and o-Al_2N_2 (1171.85/1064.25 mAh g^{-1}). Furthermore, during the insertion processes, a small volume shrinkage is observed (between −0.41% and −6.48% for Li; −0.43% and −0.46% for Na at maximum storage capacity), indicating excellent cycling stability. The remarkable combination of high specific capacity, favorable diffusion kinetics, minimal volume change, and metallic electronic character positions o-Al_2C_2 as an exceptionally promising candidate for practical battery applications. Our findings not only introduce a novel anode material but also provide insights into rational design principles for high-performance energy storage materials based on 2D orthorhombic structures. Based on these findings, the 2D o-Al_2C_2 monolayer emerges as a novel and promising candidate for use as a negative electrode material in lithium and sodium-ion batteries.

Acknowledgements

This research was performed using computational resources of HPC-MARWAN (www.marwan.ma/hpc) provided by the National Center for Scientific and Technical Research (CNRST), Rabat, Morocco.

Conflict of Interest

The authors declare no conflict of interest.

Author Contributions

Mohamed Agouri: conceptualization (lead); formal analysis (lead); writing—original draft (lead). **Ayoub Benaddi**: conceptualization (lead); investigation (lead). **Nabil Khossossi**: investigation (lead); software (lead). **Said El Filali**: investigation (lead); writing—original draft (supporting). **Abderrahman Abbassi**: supervision (lead); validation (lead). **Abdellatif Hasnaoui**: methodology (lead); supervision (equal). **Souad Taj**: supervision (lead); visualization (equal). **Bouzid Manaut**: conceptualization (supporting); validation (lead); visualization (lead).

Data Availability Statement

The data that support the findings of this study are available from the corresponding author upon reasonable request.

Keywords: 2D materials · density functional theory · electrochemical properties · Li–ion battery · Na–ion battery · o-Al_2C_2

[1] M. Amir, R. G. Deshmukh, H. M. Khalid, Z. Said, A. Raza, S. M. Muyeen, A.-S. Nizami, R. M. Elavarasan, R. Saidur, K. Sopian, *J. Energy Storage* **2023**, *72*, 108694.
[2] Y. Sun, N. Liu, Y. Cui, *Nat Energy* **2016**, *1*, 616.
[3] J.-M. Tarascon, M. Armand, *Nature* **2001**, *414*, 359.
[4] Y. Chen, Y. Kang, Y. Zhao, L. Wang, J. Liu, Y. Li, Z. Liang, X. He, X. Li, N. Tavajohi, B. Li, *J. Energy Chem.* **2021**, *59*, 83.
[5] S. Chavan, B. Venkateswarlu, M. Salman, J. Liu, P. Pawar, S. W. Joo, G. S. Choi, S. C. Kim, *Int. J. Heat Mass Transf.* **2024**, *232*, 125918.
[6] M. D. Slater, D. Kim, E. Lee, C. S. Johnson, *Adv. Funct. Mater.* **2013**, *23*, 947.
[7] A. Kumar Prajapati, A. Bhatnagar, *J. Energy Chem.* **2023**, *83*, 509.
[8] T. Zhang, F. Ran, *Adv. Funct. Mater.* **2021**, *31*, 2010041.
[9] W. Xu, J. Wang, F. Ding, X. Chen, E. Nasybulin, Y. Zhang, J.-G. Zhang, *Energy Environ. Sci.* **2014**, *7*, 513.

[10] S. P. Ong, V. L. Chevrier, G. Hautier, A. Jain, C. Moore, S. Kim, X. Ma, G. Ceder, *Energy Environ. Sci.* **2011**, *4*, 3680.
[11] H. G. Ali, K. Khan, M. B. Hanif, M. Z. Khan, I. Hussain, M. S. Javed, H. A. Z. Al-Bonsrulah, M. Mosiałek, M. Fichtner, M. Motola, *J. Energy Storage* **2023**, *73*, 108980.
[12] L. Peng, Y. Zhu, D. Chen, R. S. Ruoff, G. Yu, *Adv. Energy Mater.* **2016**, *6*, 1600025.
[13] J. Zheng, Z. Ren, P. Guo, L. Fang, J. Fan, *Appl. Surf. Sci.* **2011**, *258*, 1651.
[14] M. R. Al Hassan, A. Sen, T. Zaman, M. S. Mostari, *Today Chem.* **2019**, *11*, 225.
[15] B. Mortazavi, A. Dianat, O. Rahaman, G. Cuniberti, T. Rabczuk, *J. Power Sources* **2016**, *329*, 456.
[16] Q. Li, C.-G. Duan, X. Wan, J.-L. Kuo, *J. Phys. Chem. C* **2015**, *119*, 8662.
[17] S. Sun, C. Liao, A. M. Hafez, H. Zhu, S. Wu, *J. Chem. Eng.* **2018**, *338*, 27.
[18] X. Sun, Z. Wang, *Nanotechnol.* **2017**, *8*, 2711.
[19] P. U. Nzereogu, A. D. Omah, F. I. Ezema, E. I. Iwuoha, A. C. Nwanya, *Appl. Surf. Sci.* **2022**, *9*, 100233.
[20] J. Asenbauer, T. Eisenmann, M. Kuenzel, A. Kazzazi, Z. Chen, D. Bresser, *Sustain. Energy. Fuels* **2020**, *4*, 5387.
[21] Md. H. Hossain, M. A. Chowdhury, N. Hossain, Md. A. Islam, Md. H. Mobarak, *Chem. Eng. J. Adv.* **2023**, *16*, 100569.
[22] C. K. Chan, X. F. Zhang, Y. Cui, *Nano Lett.* **2008**, *8*, 307.
[23] G. A. Tritsaris, E. Kaxiras, S. Meng, E. Wang, *Nano Lett.* **2013**, *13*, 2258.
[24] E. Frackowiak, S. Gautier, H. Gaucher, S. Bonnamy, F. Beguin, *Carbon* **1999**, *37*, 61.
[25] H. Şahin, S. Cahangirov, M. Topsakal, E. Bekaroglu, E. Akturk, R. T. Senger, S. Ciraci, *Phys. Rev. B* **2009**, *80*, 155453.
[26] L. Song, L. Ci, H. Lu, P. B. Sorokin, C. Jin, J. Ni, A. G. Kvashnin, D. G. Kvashnin, J. Lou, B. I. Yakobson, P. M. Ajayan, *Nano Lett.* **2010**, *10*, 3209.
[27] M. Topsakal, E. Aktürk, S. Ciraci, *Phys. Rev. B* **2009**, *79*, 115442.
[28] A. Hosseinian, S. Soleimani-Amiri, S. Arshadi, E. Vessally, L. Edjlali, *Phys. Lett* **2017**, *381*, 2010.
[29] A. Sengupta, *Appl. Surf. Sci.* **2018**, *451*, 141.
[30] S. Ullah, P. A. Denis, F. Sato, *Appl. Surf. Sci.* **2019**, *471*, 134.
[31] A. Elomrani, M. Lamhani, S. Oukahou, K. Sbiaai, S. Lebègue, A. Hasnaoui, *Mater. Chem. Phys.* **2022**, *275*, 125191.
[32] N. Khossossi, A. Banerjee, Y. Benhouria, I. Essaoudi, A. Ainane, R. Ahuja, *Phys. Chem. Chem. Phys.* **2019**, *21*, 18328.
[33] D. Chodvadiya, U. Jha, P. Śpiewak, K. J. Kurzydłowski, P. K. Jha, *Appl. Surf. Sci.* **2022**, *593*, 153424.
[34] J. Zhao, H. Zeng, G. Yao, *Phys. Chem. Chem. Phys.* **2021**, *23*, 3771.
[35] N. Khossossi, W. Luo, Z. Haman, D. Singh, I. Essaoudi, A. Ainane, R. Ahuja, *Nano Energy* **2022**, *96*, 107066.
[36] W.-C. Sun, S.-S. Wang, S. Dong, *J. Mater. Sci.* **2021**, *56*, 13763.
[37] M. Agouri, A. Benaddi, A. Elomrani, N. Khossossi, A. Abbassi, A. Hasnaoui, B. Manaut, S. Taj, M. Driouich, *J. Energy Storage* **2024**, *94*, 112351.
[38] A. Benaddi, A. Elomrani, M. Lamhani, S. Oukahou, M. Maymoun, M. Y. Fatihi, A. Hasnaoui, *Sustain. Energy. Fuels* **2024**, *8*, 1719.
[39] E. K. U. Gross, R. M. Dreizler, *Density Functional Theory*, Springer Science & Business Media, Series B: Physics **1993**, *337*.
[40] P. Giannozzi, O. Andreussi, T. Brumme, O. Bunau, M. Buongiorno Nardelli, M. Calandra, R. Car, C. Cavazzoni, D. Ceresoli, M. Cococcioni, N. Colonna, I. Carnimeo, A. Dal Corso, S. De Gironcoli, P. Delugas, R. A. Distasio, A. Ferretti, A. Floris, G. Fratesi, G. Fugallo, R. Gebauer, U. Gerstmann, F. Giustino, T. Gorni, J. Jia, M. Kawamura, H.-Y. Ko, A. Kokalj, E. Küçükbenli, M. Lazzeri, M. Marsili, N. Marzari, F. Mauri, N. L. Nguyen, H.-V. Nguyen, A. Otero-De-La-Roza, L. Paulatto, S. Poncé, D. Rocca, R. Sabatini, B. Santra, M. Schlipf, A. P. Seitsonen, A. Smogunov, I. Timrov, T. Thonhauser, P. Umari, N. Vast, X. Wu, S. Baroni, *J. Phys.: Condens. Matter* **2017**, *29*, 465901.
[41] J. Paier, R. Hirschl, M. Marsman, G. Kresse, *J. Chem Phys.* **2005**, *122*, 234102.
[42] P. E. Blöchl, *Phys. Rev. B* **1994**, *50*, 17953.
[43] S. Grimme, *J. Comput. Chem.* **2006**, *27*, 1787.
[44] G. Henkelman, A. Arnaldsson, H. Jónsson, *Comput. Mater. Sci.* **2006**, *36*, 354.
[45] K. Momma, F. Izumi, *J. Appl. Cryst.* **2011**, *44*, 1272.
[46] A. Kokalj, *Comp. Mater. Sci.* **2003**, *28*, 155.
[47] A. Togo, L. Chaput, T. Tadano, I. Tanaka, *J. Phys.: Condens. Matter.* **2023**, *35*, 353001.
[48] Q. He, B. Yu, Z. Li, Y. Zhao, *Mater.* **2019**, *2*, 264.
[49] G. Henkelman, B. P. Uberuaga, H. Jónsson, *J. Chem. Phys.* **2000**, *113*, 9901.
[50] Y. J. Dappe, R. Oszwaldowski, P. Pou, J. Ortega, R. Pérez, F. Flores, *PRB* **2006**, *73*, 235124.
[51] N. D. Drummond, V. Zólyomi, V. I. Fal'ko, *Phys. Rev. B* **2012**, *85*, 075423.
[52] W. Hu, J. Yang, *J. Phys. Chem. C* **2015**, *119*, 20474.
[53] L. Meng, S. Ni, M. Zhou, Y. Zhang, Z. Li, W. Wu, *Phys. Chem. Chem. Phys.* **2017**, *19*, 32086.
[54] L. Hu, X. Wu, J. Yang, *Nanoscale* **2016**, *8*, 12939.
[55] N. Khossossi, A. Banerjee, I. Essaoudi, A. Ainane, P. Jena, R. Ahuja, *J. Power Sources* **2021**, *485*, 229318.
[56] M. Wan, Z. Zhang, Y. Peng, S. Zhao, N. Zhou, *J. Solid State Chem.* **2023**, *327*, 124284.
[57] S. Schweidler, L. de. Biasi, A. Schiele, P. Hartmann, T. Brezesinski, J. Janek, *J. Phys. Chem. C* **2018**, *122*, 8829.
[58] Y. Wang, Y. Li, *J. Mater. Chem. A* **2020**, *8*, 4274.
[59] X. Lv, F. Li, J. Gong, J. Gu, S. Lin, Z. Chen, *Phys. Chem. Chem. Phys.* **2020**, *22*, 8902.
[60] Y. Kuai, C. Chen, S. Gao, W. Chen, J. Hao, G. Wu, F. Chen, S. Guo, L. Wu, P. Lu, *Appl. Surf. Sci.* **2022**, *586*, 152510.
[61] T. Baba, K. Sodeyama, Y. Kawamura, Y. Tateyama, *Phys. Chem. Chem. Phys.* **2020**, *22*, 10764.
[62] R. Yazami, Y. Reynier, *Electrochimica Acta* **2002**, *47*, 1217.
[63] L. Zhao, Y. Wang, C. Wei, X. Huang, X. Zhang, G. Wen, *Particuology* **2024**, *87*, 240.
[64] H. Liu, D. Su, R. Zhou, B. Sun, G. Wang, S. Z. Qiao, *Adv. Energy Mater.* **2012**, *2*, 970.
[65] T. Han, Y. Liu, X. Lv, F. Li, *Phys. Chem. Chem. Phys.* **2022**, *24*, 10712.
[66] D. Wang, Y. Liu, X. Meng, Y. Wei, Y. Zhao, Q. Pang, G. Chen, *J. Mater. Chem. A* **2017**, *5*, 21370.
[67] S. J. An, J. Li, C. Daniel, D. Mohanty, S. Nagpure, D. L. Wood, *Carbon* **2016**, *105*, 52.
[68] Z. Wang, G. Zhang, Y. Wang, C. Huang, Y. Liu, C. Ouayng, J. Hu, *Appl. Surf. Sci.* **2022**, *593*, 153354.
[69] S. Ma, H. Zhang, Z. Cheng, X. Xie, X. Zhang, G. Liu, G. Chen, *Appl. Surf. Sci.* **2024**, *648*, 159024.

Manuscript received: January 13, 2025
Revised manuscript received: March 27, 2025
Version of record online: